Phase stability and shear softening in $CaSiO_3$ perovskite at high pressure

Lars Stixrude and C. Lithgow-Bertelloni
Department of Geological Sciences, University of Michigan, Ann Arbor, Michigan, USA

B. Kiefer
Department of Physics, New Mexico State University, Las Cruces, New Mexico, USA

P. Fumagalli
Dipartimento di Scienze della Terra, Universitá degli Studi di Milano, Milan, Italy
(Received 22 June 2006; revised manuscript received 4 November 2006; published 12 January 2007)

We predict the phase diagram of $CaSiO_3$ perovskite, finding the tetragonal $I4/mcm$ structure transforming to cubic $Pm\bar{3}m$ with increasing temperature. The transition temperature is 1150 K at 0 GPa, and 2450 K at 140 GPa. The c/a ratio of the tetragonal structure is 1.018 at 100 GPa and increases on compression, as does the static enthalpy difference between tetragonal and cubic structures. The elastic constants of the tetragonal phase at static conditions differ substantially from those of the cubic phase with the Voigt-Reuss-Hill shear modulus 29% less at 100 GPa. Computations are based on density functional theory in the local density and generalized gradient approximations. The phase diagram and high temperature elastic constants are computed using a mean field theory with parameters of the Landau potential determined via structurally constrained density functional theory calculations. We present a simple scheme for systematically searching for the ground state over all perovskite structures derivable from octahedral rotations within the context of symmetry-preserving relaxation, which confirms tetragonal $I4/mcm$ as the ground state in density functional theory. We argue that the experimental x-ray diffraction pattern can be explained by the $I4/mcm$ phase by considering the development of preferred orientation under uniaxial compression.

DOI: 10.1103/PhysRevB.75.024108 PACS number(s): 61.50.Ks, 62.20.Dc

I. INTRODUCTION

Among the perovskite structured oxides are materials exhibiting technologically important properties such as high temperature superconductivity,[1] colossal magnetoresistance,[2] ferroelectricity,[3] and superionic conductivity.[4] Such a variety of disparate physical behavior originates in the remarkable flexibility of the perovskite structure in accommodating cations with a wide range of radii and valences. The relative sizes of the two cations conform to the Goldschmidt tolerance factor $t=(r_O+r_A)/\sqrt{2}(r_O+r_B)\approx 1$ where the A cation occupies a larger site that is 12-fold coordinated in the ideal cubic structure and the B cation occupies a smaller octahedrally coordinated site.[5] When $t<1$ the octahedra rotate, driven by soft phonon modes at the Brillouin zone boundary,[6] reducing the value of the interoctahedral B-O-B angle to less than 180°, and producing ferroelastic distortions.[7]

The name perovskite derives from the naturally occurring mineral of $CaTiO_3$ composition,[8] but the structure is geologically most important as that of high pressure silicate phases that are thought to be the most abundant in the Earth.[9] The lower mantle, extending from 660 km to 2900 km depth (24–136 GPa) is composed almost entirely of two perovskites of ideally $MgSiO_3$ and $CaSiO_3$ composition with little intersolubility. The contrast in elastic properties between these two phases might be used to constrain the chemical composition of the deep Earth by comparing to seismologically determined elastic wave velocities.[10]

The structure of $CaSiO_3$ perovskite remains a major uncertainty with important geophysical implications since phase transitions associated with even subtle octahedral rotations are known to produce large elastic anomalies.[11] Whereas experiments find a tetragonal structure with $c/a<1$ (Refs. 12 and 13), density functional theory also predicts a tetragonal ground state ($I4/mcm$) but with $c/a>1$ (Refs. 14–16).

Resolving the apparent discrepancy between theory and experiment is critical for understanding elasticity since the experimentally observed distortion is not ferroelastic. There are as yet no measurements of the elastic constants of $CaSiO_3$ perovskite other than the bulk modulus.[17] Only the elastic constants of the cubic phase have been predicted via density functional theory.[18]

We apply density functional theory in a different way to face the challenges of a high pressure system in which the energetics of phase stability are subtle and intrinsically anharmonic: the quasiharmonic approximation, which has been used to investigate many other high pressure phase transformations and elasticity,[19] does not apply. Because of the apparent discrepancy between theory and experiment, we reexamine the identity of the ground state in density functional theory using a systematic search strategy over all possible structures derivable from octahedral rotations. Having confirmed the ground state as $I4/mcm$, we predict its elastic constants and find large differences as compared with the cubic structure. The stability field of the shear-softened tetragonal phase is found to overlap with pressure-temperature conditions of Earth's interior via an effective Hamiltonian with parameters determined by structurally constrained density functional theory calculations.

II. METHODS

A. Density functional theory

Calculations are based on density functional theory with the projector augmented wave (PAW) method.[20] Computations are performed with VASP (Ref. 21) at static (0 K) conditions. We focus on the local density approximation (LDA) since this yields better agreement with the experimental equation of state, but also perform limited calculations within the generalized gradient approximation (GGA). At each volume, the structure is fully relaxed: atomic positions and lattice parameters are adjusted until net forces and nonhydrostatic stresses vanish. The PAW potentials are harder and presumably more representative of the all-electron limit as compared with previous studies:[15,16] for Ca we use a core electronic configuration $1s^2 2s^2 2p^6$ and core radius $R_{Ca}=2.3$ Bohr; for Si $1s^2 2s^2 2p^6$, $R_{Si}=1.6$ Bohr; and for oxygen $1s^2$, $R_O=1.1$ Bohr.

The harder PAW potentials necessitate an energy cutoff $E_{cut}=1000$ eV, for which the Pulay stress is less than 1 GPa and the total energy difference between cubic and ground state structures is converged to better than 2 meV. In all calculations with unit cells containing 20 atoms, including all elastic constant calculations, we used a $4\times4\times4$ k-point mesh. In calculations with 40 atom unit cells, we used a $2\times2\times2$ mesh. Larger k-point meshes changed the total energy difference by less than 1 meV. Differences in total energy are always taken from calculations using the same size unit cell and the same k-point mesh for both structures.

The method of computation of the elastic constant tensor follows previous work.[22] Once the equilibrium structure at a given volume is found, the structure is strained, and the stress tensor recomputed. Atomic positions are rerelaxed in the strained configuration. A minimal set of longitudinal and shear strains of ±0.25% are applied. The elastic constants are then given by the appropriate ratios of deviatoric stress to applied strain.

B. Systematic search strategy for the ground state structure

Assuming that the octahedra be essentially rigid and that the translational repeat unit not exceed two octahedra in each direction, Ref. 23 derived 15 possible symmetrically distinct space groups by octahedral rotations. They found that all known perovskite structures with tilting distortions belonged to one of these 15 space groups. They further derived the subgroup-supergroup relations among these structures, which are schematically illustrated in Fig. 1.

We performed a systematic search for the ground state that takes advantage of the properties of symmetry-preserving relaxation. This kind of relaxation is a common feature of density functional theory based codes because explicit symmetrization of the wave functions, forces, and stresses increases the efficiency. As a result, all symmetry elements present in the initial structure are preserved during the course of the relaxation. New symmetry elements may develop if these lower the total energy. This means that in the scheme of Fig. 1 symmetry-preserving relaxation is unidirectional: starting from any particular space group, relaxation

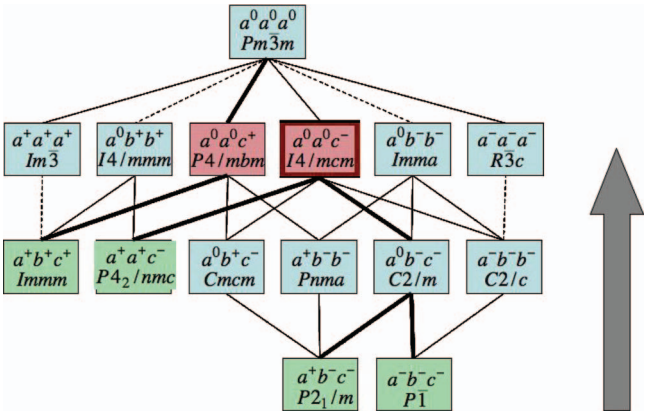

FIG. 1. (Color) Schematic representation of space groups derivable by octahedral rotations from the cubic parent structure ($Pm\bar{3}m$). Lines represent subgroup-supergroup relationships and are dashed when Landau theory predicts a first order transition. Structures are also identified by the pattern of octahedral rotation in the notation of Glazer (Ref. 56) cubic axes are labeled a,b,c, and the tilt about each axis by the symbols 0, +, −, to indicate, respectively, no rotation or rotation of successive planes of octahedra in the same (M point) or in the opposite sense (R point). The minimal subgroups are colored green and represent the starting point for our systematic search. End points of symmetry-preserving relaxations are colored red. The bold outline indicates the lowest energy of these end points, identifying tetragonal $I4/mcm$ as the ground state. Bold black lines schematically illustrate possible paths followed by symmetry-preserving relaxation from initial to final structures. After Refs. 23 and 57.

can either leave the structure unchanged, if it is the ground state, or it can move upwards along subgroup-supergroup relations if these lower the total energy. Our symmetry-preserving relaxation permits all structural distortions consistent with the initial space group that lower the total energy, including octahedral distortions and cation displacements, in addition to octahedral rotation. Complete relaxation is essential, particularly in a system such as $CaSiO_3$ in which energy differences from the cubic parent structure are subtle. We anticipate that our results will therefore be more accurate than those based on incomplete structural relaxation in which only octahedral rotation was considered.[24]

Our strategy is as follows. We initiate structural relaxations from each of the four minimal subgroups: $Immm$, $P4_2/nmc$, $P2_1/m$, and $P\bar{1}$. We used a $2\times2\times2$ supercell (40 atoms), which is essential to our strategy because it is the minimal translational unit that can represent all fifteen structures commensurately. Initial structures corresponding to each of these space groups are prepared by rotating octahedra small finite amounts (7°–11°).

C. Mean field theory

In order to investigate high-temperature elasticity and phase stability, we make use of a mean field theory with parameters constrained by first principles calculations. The Landau potential governing perovskite structures related by octahedral rotations at the R point on the Brillouin zone boundary is[25]

$$G = \frac{1}{2}a(1 - T/T_C)(q_1^2 + q_2^2 + q_3^2) + \frac{1}{4}b(q_1^2 + q_2^2 + q_3^2)^2 + \frac{1}{4}b'(q_1^4 + q_2^4 + q_3^4) + \frac{1}{6}c(q_1^2 + q_2^2 + q_3^2)^3 + \frac{1}{6}c'(q_1^2 q_2^2 q_3^2) + \frac{1}{6}c''(q_1^2 + q_2^2 + q_3^2)(q_1^4 + q_2^4 + q_3^4) + \lambda_2[\sqrt{3}e_o(q_1^2 - q_2^2) + e_t(2q_3^2 - q_1^2 - q_2^2)] + \lambda_3(e_4 q_2 q_3 + e_5 q_1 q_3 + e_6 q_1 q_2) + \frac{1}{2}[(c_{11}^0 - c_{12}^0)(e_t^2 + e_o^2) + c_{44}^0(e_4^2 + e_5^2 + e_6^2)], \quad (1)$$

where q_i is the octahedral rotation about axis i, the elastic constants c_{ij}^0 are those of the cubic structure, e_i are the elements of the strain tensor with the symmetry adapted combinations $e_o=(e_1-e_2)/\sqrt{2}$, $e_t=(2e_3-e_1-e_2)/\sqrt{6}$, and we have neglected pure volumetric strain. In addition to the cubic phase, we will pay particular attention to the tetragonal $I4/mcm$ phase, with nonzero q_3 and e_t, and the orthorhombic *Imma* phase, with nonzero $q_2=q_3$, e_t, e_o, and e_4.

We find the values of the parameters appearing in the Landau potential [Eq. (1)] by fitting to a series of unrelaxed density functional theory calculations for several fixed values of q_i and e_i. These calculations were all performed in a $2\times2\times2$ supercell with initially cubic atomic coordinates and lattice parameters. Oxygens were displaced according to several fixed values of q_i. We take $q_i=\delta_x$ the change in the fractional oxygen coordinate relative to the cubic parent structure along the R-point soft-mode eigenvector. Lattice parameters were altered according to several fixed values of the strains. In order to constrain the coupling constants we consider cases in which two or more of the relevant structural quantities (q_1,q_2,q_3,e_t,e_o) are set to nonzero values. Further details concerning the values chosen are found below in Sec. III.

The elastic constants of the distorted phase are related to those of the cubic phase by[7]

$$c_{ij} = c_{ij}^0 - \frac{\partial^2 G}{\partial e_i \partial q_m}\chi_{mn}\frac{\partial^2 G}{\partial e_j \partial q_n}, \quad (2)$$

where

$$\chi_{mn}^{-1} = \frac{\partial G}{\partial q_m \partial q_n} \quad (3)$$

and the derivatives are evaluated at equilibrium.

In the displacive limit the Landau potential is related to the underlying microscopic Hamiltonian[26–28]

$$\mathcal{H} = \sum_{\alpha}^{N}\frac{1}{2}(p_3^{\alpha})^2 + V_s(q_3^{\alpha}) + \frac{J}{2}\sum_{\beta}^{nn}(q_3^{\alpha} + q_3^{\beta})^2, \quad (4)$$

where we have focused on the primary order parameter of the phase transition from tetragonal $I4/mcm$ to cubic, $q_3=\langle q_3^{\alpha}\rangle$ and the brackets indicate the ensemble (thermodynamic) average. The conjugate momenta are p_3^{α}, N is the number of sites (octahedra), J is the intersite coupling constant, and the second sum is over nearest neighbors only. The form of the intersite coupling: a sum, rather than a difference of nearest neighbor rotations as is more commonly written, is that appropriate for a transition driven by a zone-boundary mode. The coefficients of the on-site term

$$V_s = \frac{1}{2}Aq_3^2 + \frac{1}{4}Bq_3^4 + \frac{1}{6}Cq_3^6 \quad (5)$$

are related to those of the Landau potential: $A=a$, $B=b+b'$, $C=c+c''$.

The critical temperature is related to the excess enthalpy of the distorted phase ΔH via the depth of the on-site potential well[26,29]

$$k_B T_C = 0.440\frac{\Delta H}{s} \quad (6)$$

and the coefficient is known from Monte Carlo simulations. The value of $s=|A|/24J$ is determined by the dispersion of the unstable-mode branch along $\Gamma-R$ (Ref. 14)

$$\omega^2(\Lambda) = A + 12J(1 + \cos\pi\Lambda), \quad (7)$$

where the octahedral rotations are modulated with wave vector $\frac{2\pi}{a}\Lambda(\frac{1}{2},\frac{1}{2},\frac{1}{2})$ and the scalar Λ varies from zero at the Brillouin zone center (Γ) to unity at the R point. For $CaSiO_3$ perovskite, Ref. 14 found that the dispersion scales with the frequency so that $s=0.071$, essentially independent of compression. The fact that $s\ll1$ indicates that the transition occurs in the displacive limit.

III. RESULTS

A. Ground state

A systematic search at $V=35$ Å^3 per $CaSiO_3$ reveals $I4/mcm$ as the ground state. Relaxations initiated with minimal subgroups with at least one out-of-phase rotation $(P4_2/nmc, P2_1/m, P\bar{1})$ all yielded the tetragonal structure $I4/mcm$ with identical lattice vectors, atomic coordinates, and total energies. The remaining minimal subgroup *Immm* instead relaxed to tetragonal $P4/mbm$ with very slight distortion and significantly higher total energy than for the $I4/mcm$ structure, by 28 meV per formula. *Immm* is unique among the four minimal subgroups in not having $I4/mcm$ as a supergroup (Fig. 1). Since there is no line connecting *Immm* to the ground state $I4/mcm$, the relaxation continues until the lowest energy supergroup is found, which in this case turns out to be $P4/mbm$. Since all minimal subgroups that are permitted to yield $I4/mcm$ via symmetry-preserving relaxation did in fact yield this structure, and since this was the lowest energy structure found, all other space groups are excluded as ground-state structures.

These results are in excellent agreement with those of other studies that also conclude that $I4/mcm$ is the ground state based on an analysis of a subset of possible structures.[15,16] Another study,[24] which found a different structure (*Pnma*), used a different electronic structure method and did not fully relax the structure.

Our relaxation strategy reveals another important aspect of the relative stability of the various structures. Symmetry preserving relaxations performed in smaller unit cells can become trapped in local minima that may represent

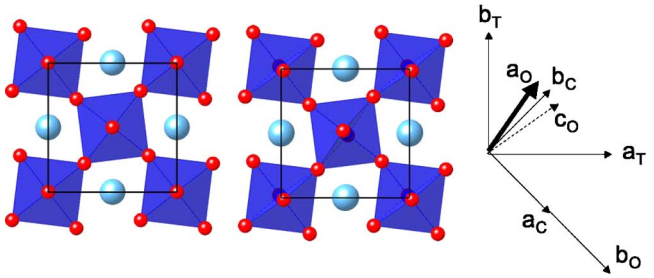

FIG. 2. (Color online) Comparison of the tetragonal $I4/mcm$ structure in the equilibrium state (left) and upon application of $e_4=0.02$ (middle), where the strain is referred to the cubic reference frame (right). These views are down the tetragonal (and cubic) c axis and show the q_3 rotation in both cases. An additional rotation about the cubic b axis (q_2) is excited by the shear. At right is a comparison of the $Pm\bar{3}m$ (subscript C), $I4/mcm$ (T), and $Imma$ (O) lattice vectors. A change in c/a in the tetragonal frame corresponds to an e_5 strain in the orthorhombic frame. The orthorhombic lattice vectors in the cubic frame are $a_O=(011)$, $b_O=(200)$, $c_O=(01\bar{1})$.

elastically unstable saddle points. For example, the *Imma* structure is elastically unstable at high pressure. Symmetry preserving relaxation initiated with conventional 20 atom unit cells in *Imma* cannot yield $I4/mcm$. The excited state is related to the ground state by a shear strain (e_5 in the *Imma* coordinate frame) that is forced to vanish during the symmetry-preserving relaxation (Fig. 2). The elastic instability can only be revealed by relaxing in the translationally unrestricted $2\times2\times2$ supercell which does relax to the correct ground state ($I4/mcm$), or by applying the e_5 strain and breaking the symmetry.

B. Energetics, structure, and equation of state

The energy and enthalpy differences between the ground state ($I4/mcm$) and cubic structures increase on compression

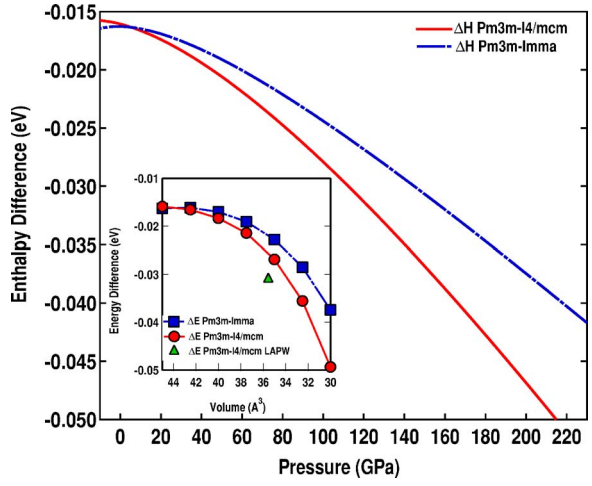

FIG. 3. (Color online) Enthalpy differences between tetragonal $I4/mcm$ and cubic $Pm\bar{3}m$ (solid), and between orthorhombic *Imma* and cubic (dashed) as a function of pressure. The inset shows the total energy differences as a function of volume compared with the $I4/mcm$-cubic all-electron result (Ref 14).

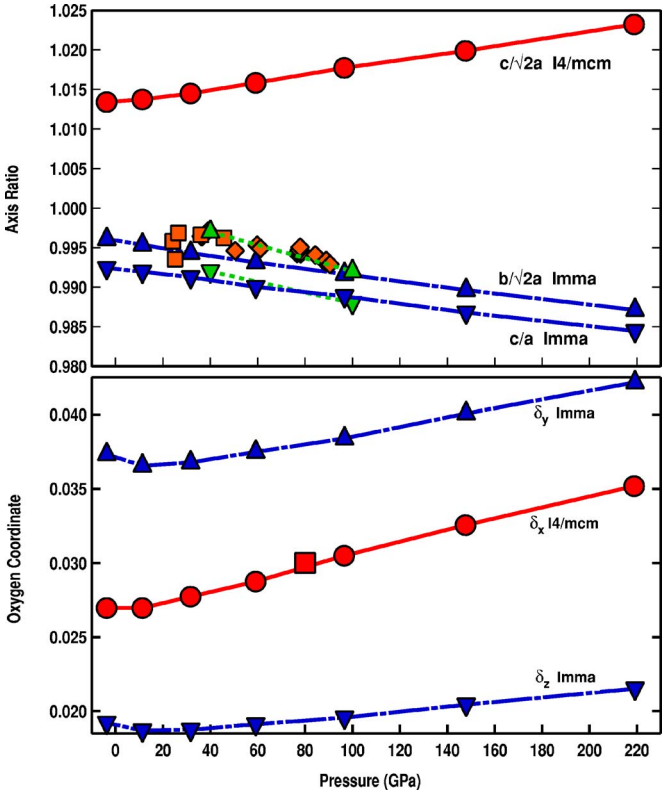

FIG. 4. (Color online) Lattice parameter ratios (top) and oxygen coordinates (bottom) for tetragonal $I4/mcm$ (circles) and orthorhombic *Imma* (triangles). The square in the bottom figure shows the all electron result (Ref. 14). The oxygen coordinate for $I4/mcm$ is represented by $\delta_x=x_O-1/4$ and those for *Imma* by $\delta_y=y_O$ and $\delta_z=z_O$. In the top panel, red symbols show experimental data (Refs. 12 and 13), and green triangles show the results of static GGA PAW calculations (Ref. 44).

(Fig. 3). The energy difference between these two structures at $V=35$ Å^3 (28 meV) is considerably smaller than that found in a recent pseudopotential calculation at the same volume[16] (74 meV), but agrees well with the previous all electron result[14] (31 meV at $V=35.6$ Å^3). The greater accuracy of the PAW result as compared with all electron calculations is expected. The smaller energy difference found in a recent study[15] is due to the different exchange-correlation potential (19 meV, GGA). The energy difference between $I4/mcm$ and *Imma* structure also increases on compression to 4 meV at $V=35$ Å^3 (Fig. 3). *Imma* has the lowest enthalpy at pressures below 5 GPa, well below the thermodynamic stability field of perovskite.

The deviation of the ground-state structure from cubic increases with increasing pressure (Fig. 4). The lattice parameter ratio $c/\sqrt{2}a$ increases from 1.013 at zero pressure to 1.020 at 140 GPa. The oxygen coordinate $x_O=1/4+\delta_x$, related to the octahedral rotation angle ϕ by $\sin\phi=4\delta_x$, also increases with increasing pressure and agrees with that found in the all electron study.[14]

The equations of state of the three structures $Pm\bar{3}m$, *Imma*, and $I4/mcm$ are nearly identical (Fig. 5). A fit to our results with the Birch-Murnaghan finite strain theory[30] yields $V_0=44.0$ Å^3, $K_0=252$ GPa, $K_0'=4.1$, in excellent

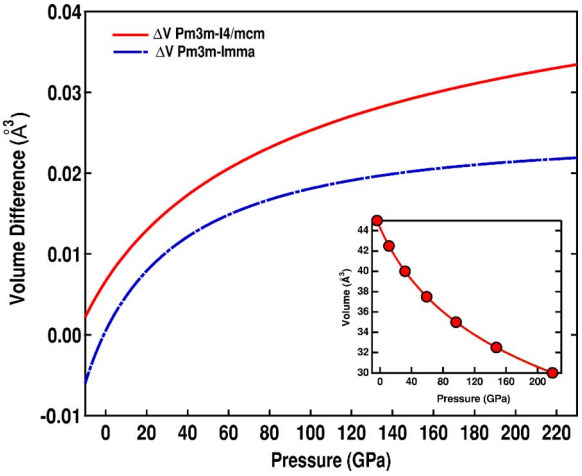

FIG. 5. (Color online) Volume difference between tetragonal $I4/mcm$ and cubic $Pm\bar{3}m$ (solid) and between orthorhombic *Imma* and cubic (dashed) as a function of pressure. The inset shows the equation of state of the three phases which are indistinguishable on this scale.

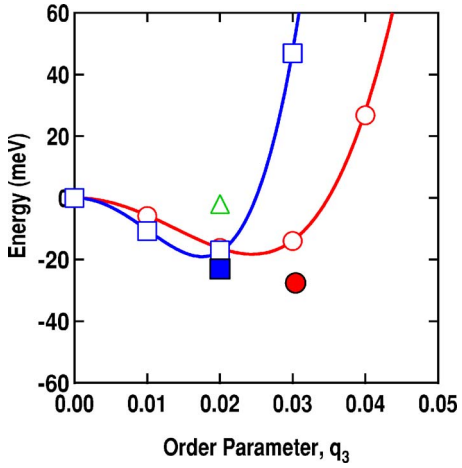

FIG. 6. (Color online) Calculations used to determine the value of the Landau potential parameters at $V=35$ Å^3 with $q_3 \neq 0$ (open circles), $q_2=q_3 \neq 0$ (open squares), and $q_1=q_2=q_3 \neq 0$ (triangle). The solid circle represents the ground state. In the calculation represented by the solid square the atomic positions were fixed at $q_2=q_3=0.02$ and the lattice was allowed to relax to a state of hydrostatic stress.

agreement with previous LDA results.[16] The value of V_0 is slightly smaller ($\sim 3\%$) and the value of K_0 slightly larger ($\sim 0-6\%$) than a range of recent experimental values,[12,13,17] consistent with the anticipated effects of phonon excitation.[31] The $I4/mcm$ structure has the smallest volume and the cubic phase has the largest volume at all pressures. These trends are consistent with the evolution of the enthalpy differences (Fig. 3) according to the thermodynamic relation: $\partial \Delta H/\partial P=\Delta V$, where ΔV is the excess volume of the distorted phase and P is the pressure.

The parameters of the Landau potential [Eq. (1)] are determined by a series of constrained density functional theory calculations (Fig. 6). At $V=35$ Å^3 these show the expected behavior as a function of q_3, with a local maximum at the origin and a minimum at $q_3=0.25$ similar to that of the ground state structure. The ground state is slightly lower in energy and has a slightly larger value of q_3 because of coupling to the tetragonal strain. Calculations with $q_2=q_3$ show similar trends although the energy is higher than that of the tetragonal structure, consistent with the results of our fully relaxed calculations. A single calculation with $q_1=q_2=q_3$ has still higher energy. The values of the parameters are shown in Table I. The phase transformation to the cubic structure is more nearly critical than tricritical, since the ratio $(b+b')^2/4a(c+c'') > 1$ (Ref. 32).

C. Elastic constants

The elastic constants of the tetragonal $I4/mcm$ ground state differ substantially from those of the cubic phase (Fig. 7). The largest relative difference is in the shear elastic constants, both of which are lower than that of the cubic structure at all pressures. Near 100 GPa, c_{44} is softened by 40% and c_{66} is softened by 14%. At lower pressures, c_{66} is softened more than c_{44}. The longitudinal (c_{11},c_{33}) and off-diagonal (c_{12},c_{13}) elastic constants are split in the lowered tetragonal symmetry in such a way that their average value is similar to that of the cubic phase, at least up to 100 GPa. The Voigt-Reuss-Hill shear modulus[33] of the tetragonal structure is much softer than that of the cubic structure, by 29% at 100 GPa (Fig. 7). In contrast, the bulk moduli of cubic and tetragonal structures are nearly identical, reflecting the negligible effect of distortion on the equation of state.

The Landau potential [Eq. (1)] captures most of the important differences between cubic and tetragonal elastic constants (Table II). The Voigt-Reuss-Hill bulk and shear moduli of the tetragonal structure agree with the density functional theory results to 1% and 4%, respectively. The largest discrepancy is for c_{66}, for which the Landau potential predicts identically zero softening. To reproduce the softening of this constant would require a higher order Landau expansion. All the other elastic constants are predicted by the Landau potential to be softer in the low symmetry phase except for c_{13}, which is considerably stiffer, as also seen in density functional theory. The elastic constants of the *Imma* structure computed from the Landau

TABLE I. Landau potential parameters. Units: keV/Å^3; volume in Å^3 per formula.

V	a	b	b'	c	c'	c''	λ_2	λ_3
30.0	−0.00579	8.09	0.648	120	10800	−867	−0.0542	−0.0794
35.0	−0.00352	5.43	0.719	85.4	2020	−594	−0.0314	−0.0481
42.5	−0.00219	2.96	1.047	95.4	3030	−421	−0.0138	−0.0155
45.0	−0.00205	2.49	1.108	93.2	3280	−398	−0.0103	−0.00756

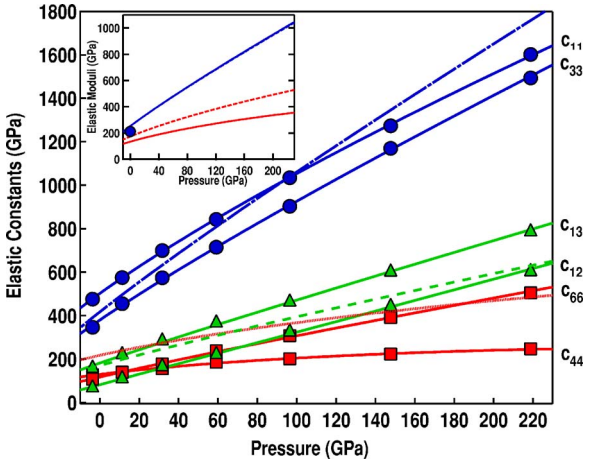

FIG. 7. (Color online) Elastic moduli of (symbols and solid line) $I4/mcm$ and (dashed lines) $Pm\bar{3}m$ structures. The identity of the moduli in the $I4/mcm$ structure are indicated along the right-hand axis. The cubic moduli are (dash-dot) c_{11}, (long-dashed) c_{12}, (short-dashed) c_{44}. The inset shows the bulk (upper curve) and shear (lower curves) for cubic (dashed) and tetragonal (solid) structures. The bulk moduli are coincident on this scale. The bulk modulus is compared (symbol) with the experimental value from the equation of state (Refs. 13 and 17).

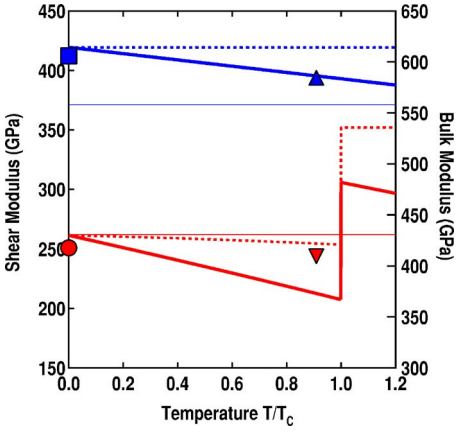

FIG. 8. (Color online) Voigt-Reuss-Hill bulk (top, right-hand axis) and shear (bottom, left-hand axis) moduli at 100 GPa as predicted by the Landau potential (bold dashed lines) and including the temperature dependence of the bare elastic constants (bold solid). Square and circle at $T=0$ are the bulk and shear moduli, respectively, computed directly from the density functional theory results for the elastic constant tensor as presented in Fig. 7. Corresponding results from a recent molecular dynamics simulation at 2000 K are shown as down- and up-pointing triangles for bulk and shear moduli, respectively (Ref. 43), and are placed on the temperature axis assuming the LAPW value (Ref. 14) for the transition temperature $T_C=2200$ K. Thin solid lines represent the bulk (upper) and shear (lower) modulus of the Earth (Ref. 58) at 100 GPa (2270 km depth).

potential show elastic instability: the value of c_{55} is negative, as anticipated from crystallographic relationships (Fig. 2).

Temperature softens the shear modulus of the tetragonal phase still further with respect to the cubic phase, while the difference in the bulk modulus between the two phases is unaffected (Fig. 8). Landau theory does not permit prediction of the temperature dependence of the bare elastic constants, i.e., those of the cubic phase. We assume, in the absence of experimental measurements, that this dependence is the same as that for $MgSiO_3$ perovskite at a similar pressure:[34] $d\mu/dT=-21$ MPa K^{-1} and $dK_S/dT=-14$ MPa K^{-1}, where μ is the shear modulus and K_S is the adiabatic bulk modulus. These values are similar to an independent estimate for $CaSiO_3$ perovksite based on systematic relations[35] (-21 MPa K^{-1} and -13 MPa K^{-1}, respectively).

D. Phase stability

The temperature of the tetragonal to cubic phase transition varies from 1150 K near 0 GPa, to 2450 K at 136 GPa, corresponding to the base of Earth's mantle (Fig. 9). These values are computed from Eq. (6) with the cubic-tetragonal enthalpy difference from density functional theory (Fig. 3) and a constant value $s=0.071$ (see discussion in Sec. II and Ref. 14). The tetragonal-cubic phase boundary lies somewhat below the earlier LAPW prediction[14] of 2200 K at 80 GPa. The LAPW value is presumably more accurate and reflects the larger energy difference between tetragonal and cubic phases than in the PAW calculations. We may estimate the influence of approximations to the exchange-correlation potential in the same spirit: the temperature of the GGA phase boundary is assumed to scale with the difference in the tetragonal-cubic energy contrast between LDA (this work) and GGA.[15]

The tetragonal to orthorhombic phase boundary is determined by computing the Gibbs free energy of the two phases according to Eq. (1) as a function of temperature and at a series of pressures by interpolating the coefficients of Table I. These calculations show that the Clapeyron slope is negative and that the tetragonal phase is stable at higher temperature than the orthorhombic phase.

The predicted Clapeyron slope of the tetragonal to cubic transition agrees with perovskite systematics.[36] In those perovskites for which the B-O bond is stiffer than the A-O bond, the Clapeyron slope is invariably positive for transitions involving octahedral tilting. The sense of curvature of the boundary is also readily understood: the volume contrast between tetragonal and cubic increases on compression (Fig.

TABLE II. Elastic constants at $V=35$ Å^3.

	K	μ	c_{11}	c_{33}	c_{12}	c_{13}	c_{44}	c_{66}
Cubic	614	353	1057	1057	393	393	367	367
Tetragonal	606	251	1036	908	315	462	203	301
Tetragonal-Landau	614	262	1017	898	353	472	216	367

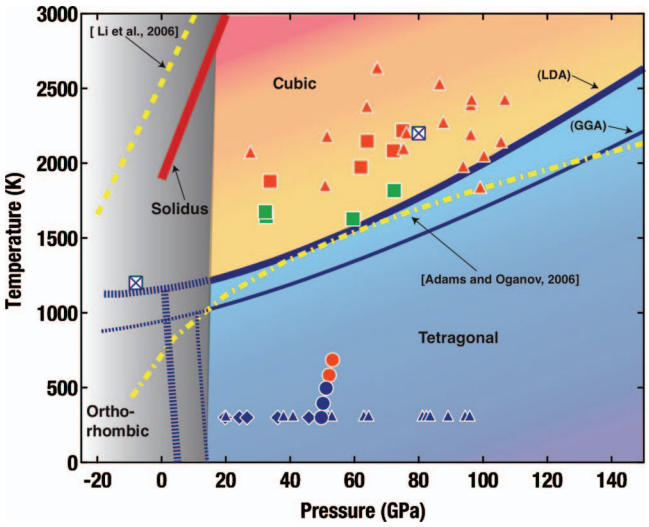

FIG. 9. (Color) Predicted $CaSiO_3$ phase diagram showing the tetragonal to cubic phase boundary in LDA (thick blue line) and GGA (thin blue). Phase boundaries are dashed within the thermodynamic stability field of nonperovskite structured phases as indicated by the black shading (Ref. 59). The orthorhombic to tetragonal transition is indicated by the nearly vertical dashed lines. Location of the transition to the cubic phase from molecular dynamics simulations are shown in yellow: dot-dashed (Ref. 44) and dashed (Ref. 51). LAPW results for the tetragonal to cubic transition (Ref. 14) are shown as crossed squares. Experimental data for the tetragonal phase in blue and cubic phase in red [diamonds (Ref. 12), triangles (Ref. 13), circles (Ref. 42)]. Squares are experimental results for a sample with 5 wt % Al_2O_3 (Ref. 42): green: orthorhombic, red: cubic. The red curve is the melting line (Ref. 60). For comparison the average temperature in the Earth at 100 GPa (2270 km depth) is 2300 K (Ref. 61), with lateral variations of several hundred degrees expected.

5), which requires the dT/dP slope of the phase boundary also to increase according to the Claussius-Clapeyron equation. The tetragonal-cubic phase boundary in $SrTiO_3$ shows the same sense of curvature.[37] The negative slope of the tetragonal to orthorhombic boundary is caused by the larger volume of the low symmetry phase: while the orthorhombic phase shows rotations about two axes, as opposed to only one in the tetragonal phase, its volume is larger because the magnitude of rotation is less.

IV. DISCUSSION

One way to understand the origin of large shear softening in the $I4/mcm$ phase is to examine the influence of strain on the structure (Fig. 2). Application of the e_4 strain lowers the symmetry and excites an additional octahedral rotation, q_2 that is not present in the ground state structure. This additional octahedral rotation softens the elastic response. The large shear softening can also be understood in terms of the Landau potential. The analytical expression for c_{44} in the limit $c=c'=c''=0$ is[7]

$$c_{44} = c_{44}^0 - \frac{\lambda_3^2}{12\lambda_2^2/(c_{11}^0 - c_{12}^0) - b'}. \quad (8)$$

The λ_3 coupling term relates e_4 to the octahedral rotation present in the ground state q_3 and an additional rotation q_2 that is excited by strain. The results of the mean field theory are thus in concert with our analysis of the strained structure.

The remarkable elastic properties of the $I4/mcm$ phase highlight the apparent discrepancy between theoretically predicted and experimentally observed structures. Our results suggest a resolution. The experimental identification rests on the observation that the $(200)_C$ diffraction line, where the subscript C indicates reference to cubic axes, is split into two peaks such that the one at larger d-spacing is more intense (Ref. 12). The key is to recognize that the experiments are under nonhydrostatic stress, even with the use of quasihydrostatic pressure media and annealing. The spontaneous strain of the ferroelastic ground state means that the elastic strain energy is minimized by orienting the long axis (c) normal to the load axis. This pattern of preferred orientation, combined with the along axis scattering geometry, would produce a more intense reflection from the larger d-spacing c axis than from the a axis, in agreement with the pattern of relative intensities observed. Strong preferred orientation of this kind would not require large stresses to develop and could be formed during the cubic-tetragonal transition, or by migration of domain walls after the formation of the tetragonal phase.[38] The preferred orientation is likely to be reproducible as temperature is cycled back and forth through the transition. Nonhydrostatic stress may influence the critical temperature.[39]

In order to test this hypothesis we simulate the x-ray diffraction pattern including the effect of preferred orientation (Fig. 10). The theoretical structure is specified by the Landau potential [Eq. (1)] with $T/T_C=0.25$, which corresponds to $T=300$ K at the experimental volume (42.4 Å^3). The influence of temperature is to diminish the distortion as compared with the static result, yielding $q_3=0.0229$ and $c/\sqrt{2}a=1.00937$. Using the March-Dollase equation[40,41] along [001] with a coefficient 0.68, matches the experimental pattern very well (Table III), with the largest discrepancy in d-spacings being 0.002 Å and the largest disagreement in relative intensities being 5%. In particular the relative intensities of the $(200)_C$ doublet (tetragonal 004 and 220) are well reproduced, as is the apparent lack of splitting (within experimental resolution) of the $(110)_C$ doublet (tetragonal 112 and 200). Since the spontaneous strain decreases linearly with temperature, finite experimental resolution may also explain undetected $(200)_C$ peak splitting at temperatures as low as 580 K in the experiments of Ref. 42.

Recent molecular dynamics simulations disagree with this picture:[43,44] *Imma* is found to be the stable structure at ambient temperature, requiring a phase transition at still lower temperatures to the tetragonal ground state. This is an unlikely scenario for two reasons. First, while $I4/mcm$ to *Imma* transitions are common in perovskites, the higher temperature phase is invariably tetragonal.[45–50] Second, the thermal energy available to drive the transition appears to be too small to overcome the $I4/mcm$-*Imma* enthalpy difference. Whereas in Ref. 44 the transition temperature was estimated as $k_BT_{tr}=\Delta H(I4/mcm\text{-}Imma)$, the displacive limit and the phonon spectrum of $CaSiO_3$ perovskite require the thermal energy substantially to exceed the enthalpy difference for the transition to proceed [Eq. (6)].

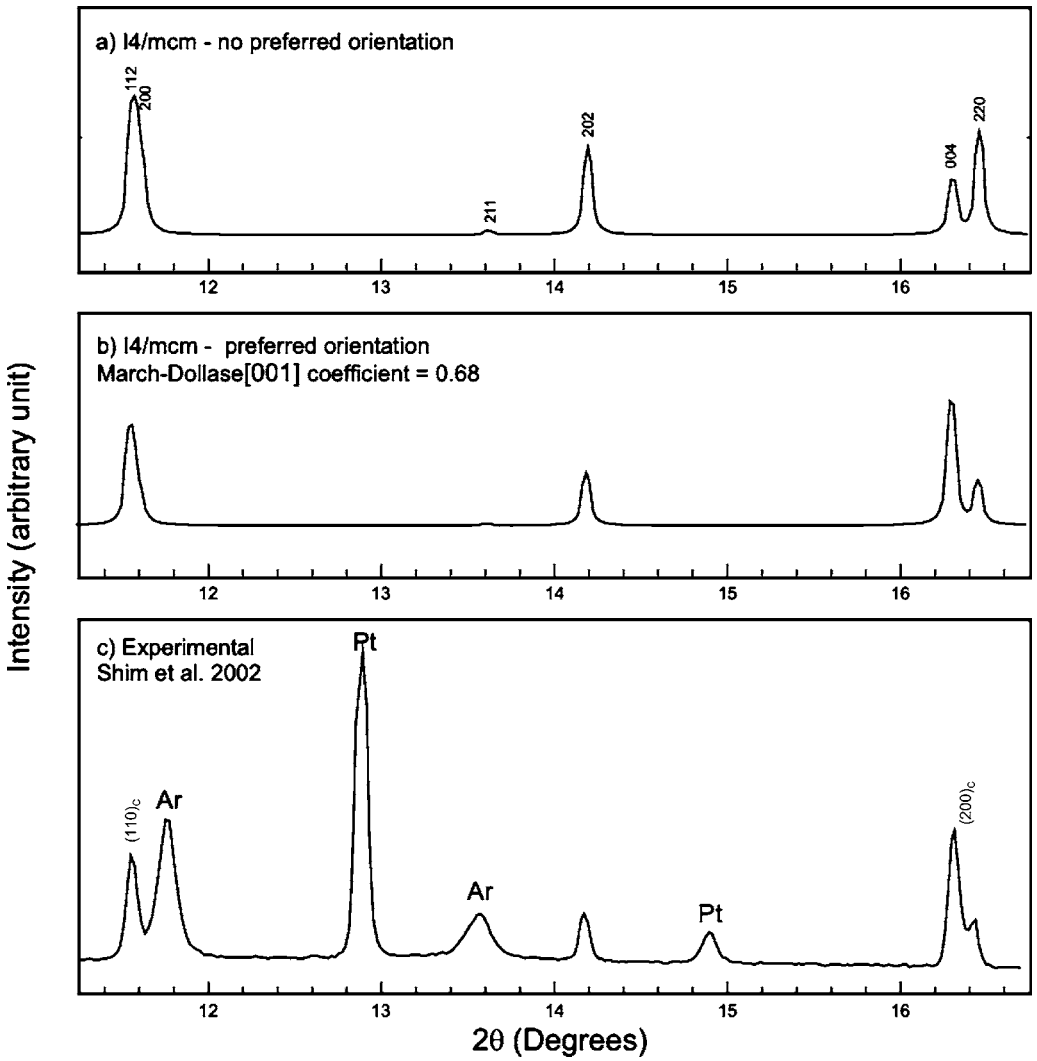

FIG. 10. Simulated x-ray diffraction pattern of the predicted 300 K $I4/mcm$ structure calculated with PowderCell (Ref. 62): (a) without any preferred orientation (b) with preferred orientation as specified by the March-Dollase equation (Refs. 40 and 41) along [001] with a coefficient of 0.68 compared with (c) experimental data at the same volume (25.2 GPa) (Ref. 12). Peaks are identified in the tetragonal frame in the upper figure and in the cubic frame (subscript C) in the lower figure.

It seems more likely that the observation of an orthorhombic phase in the molecular dynamics simulations is an artifact of finite reciprocal space sampling. The electronic structure and forces are computed at the Gamma point only in a nonequant 80-atom supercell. The Brillouin zone is sampled anisotropically, which leads to an artificial deviatoric stress.[44] A consequence of this anisotropy is that a static structural relaxation with the same computational parameters produces orthorhombic *Imma* as the ground state, in violation of fully converged calculations. It is clear then that insufficient sampling of the Brillouin zone biases the molecular dynamics simulations towards orthorhombic symmetry. Moreover, it is possible that this bias accounts entirely for the appearance of an orthorhombic phase in the molecular dynamics simulations. These limitations are likely to influence the computation of elastic constants in molecular dynamics simulations as well[51] and may account for the disagreement with our predicted high temperature elastic moduli (Fig. 8).

TABLE III. Comparison of experimental x-ray diffraction pattern at $P=25.2$ GPa, $V=42.4$ Å, $T=300$ K (Ref. 12) with that calculated theoretically at the same conditions: space group $I4/mcm$, $a=4.9145$ Å, $c=7.0153$ Å, [001] March-Dollase coefficient=0.68.

hkl	*d* theory (Å)	*d* exp. (Å)	I_{rel} theory	I_{rel} exp.
112	2.469	2.468	77	82
200	2.457	—	22	—
202	2.013	2.015	41	40
004	1.754	1.752	100	100
220	1.738	1.740	33	36

The properties of the $I4/mcm$ phase have important geophysical consequences: (i) The shear and bulk moduli are very different from those of the Earth (Fig. 8). This means that the Ca content of the lower mantle should be detectable by seismological means, allowing tests of fundamental hypotheses concerning the chemical evolution of the Earth. (ii)

According to our results, the $I4/mcm$ to cubic transition should occur at pressure-temperature conditions typical of slightly colder than average lower mantle. The large contrast in elasticity between these phases, should be observable as scattering of seismic energy.[14] Indeed, there have been persistent reports of lower mantle scatterers at depths where no other phase transformations are expected and that have never been satisfyingly explained.[52,53] (iii) The phase transition would produce an unusual signature in the lateral variations of seismic wavespeeds in the mantle. With an increase in temperature at constant depth, the shear wave velocity would increase across the transition, while the bulk sound velocity would decrease. This type of anticorrelation between shear and bulk wavespeeds is seen in several seismological Earth models in the lower mantle.[54]

V. CONCLUSIONS

Crystallographically subtle distortions at high pressure can have important geophysical consequences and may reveal features of Earth's deep interior. A slight tetragonal distortion in $CaSiO_3$ perovksite produces a large elastic anomaly that may be seismically visible in radially averaged structure, in scattering, and in lateral variations in wavespeeds. This should provide additional motivation for the first experimental measurement of the elastic constants of $CaSiO_3$ perovskite, which is challenging because the phase is unquenchable.[55] Indeed, our predicted shear modulus of $CaSiO_3$ perovskite is much lower than previous estimates and demands a reexamination of the signature of this phase in seismological observations.[10] Because the large shear softening that we find is associated with a phase transformation, experimental tests of our predicted phase diagram also become very important. We have offered a reinterpretation of the experimental x-ray diffraction pattern that reconciles these data with the prediction of density functional theory that $I4/mcm$ is the low temperature structure.

ACKNOWLEDGMENTS

We thank Sang-Heon Shim for discussions and published data. This work was supported by the National Science Foundation under grant EAR-0230154 (L.S.), the Miller Institute for Basic Research in Science (L.S.), the Elizabeth Crosby Research Fund (C.L.B.), and the David and Lucile Packard Foundation (C.L.B.).

[1] R. J. Cava, B. Batlogg, R. B. van Dover, D. W. Murphy, S. Sunshine, T. Siegrist, J. P. Remeika, E. A. Rietman, S. Zahurak, and G. P. Espinosa, Phys. Rev. Lett. **58**, 1676 (1987).
[2] A. P. Ramirez, J. Phys.: Condens. Matter **9**, 8171 (1997).
[3] R. E. Cohen, Nature (London) **358**, 136 (1992).
[4] Y. Inaguma, L. Q. Chen, M. Itoh, T. Nakamura, T. Uchida, H. Ikuta, and M. Wakihara, Solid State Commun. **86**, 689 (1993).
[5] G. H. Jonker and J. H. Vansanten, Physica (Amsterdam) **16**, 337 (1950).
[6] P. A. Fleury, J. F. Scott, and J. M. Worlock, Phys. Rev. Lett. **21**, 16 (1968).
[7] M. A. Carpenter and E. K. H. Salje, Eur. J. Mineral. **10**, 693 (1998).
[8] A. Navrotsky and D. J. Weidner, *Perovskite: A Structure of Great Interest to Geophysics and Materials Science* (American Geophysical Union, Washington, DC, 1989).
[9] R. J. Hemley and R. E. Cohen, Annu. Rev. Earth Planet Sci. **20**, 553 (1992).
[10] S. Karato and B. B. Karki, J. Geophys. Res., [Solid Earth] **106**, 21771 (2001).
[11] J. C. Slonczewski and H. Thomas, Phys. Rev. B **1**, 3599 (1970).
[12] S. H. Shim, R. Jeanloz, and T. S. Duffy, Geophys. Res. Lett. **29**, 2166 (2002).
[13] S. Ono, Y. Ohishi, and K. Mibe, Am. Mineral. **89**, 1480 (2004).
[14] L. Stixrude, R. E. Cohen, R. C. Yu, and H. Krakauer, Am. Mineral. **81**, 1293 (1996).
[15] D. Y. Jung and A. R. Oganov, Phys. Chem. Miner. **32**, 146 (2005).
[16] R. Caracas, R. Wentzcovitch, G. D. Price, and J. Brodholt, Geophys. Res. Lett. **32**, L06306 (2005).
[17] S. H. Shim, T. S. Duffy, and G. Y. Shen, J. Geophys. Res., [Solid Earth] **105**, 25955 (2000).
[18] B. B. Karki and J. Crain, Geophys. Res. Lett. **25**, 2741 (1998).
[19] J. Tsuchiya, T. Tsuchiya, and R. M. Wentzcovitch, Phys. Rev. B **72**, 020103 (2005).
[20] G. Kresse and D. Joubert, Phys. Rev. B **59**, 1758 (1999).
[21] G. Kresse and J. Furthmuller, Comput. Mater. Sci. **6**, 15 (1996).
[22] B. B. Karki, L. Stixrude, and R. M. Wentzcovitch, Rev. Geophys. **39**, 507 (2001).
[23] C. J. Howard and H. T. Stokes, Acta Crystallogr., Sect. B: Struct. Sci. **B54**, 782 (1998).
[24] B. Magyari-Kope, L. Vitos, G. Grimvall, B. Johansson, and J. Kollar, Phys. Rev. B **65**, 193107 (2002).
[25] M. A. Carpenter, A. I. Becerro, and F. Seifert, Am. Mineral. **86**, 348 (2001).
[26] A. D. Bruce, Adv. Phys. **29**, 111 (1980).
[27] S. Radescu, I. Etxebarria, and J. M. Perezmato, J. Phys.: Condens. Matter **7**, 585 (1995).
[28] E. K. H. Salje, S. A. Hayward, and W. T. Lee, Acta Crystallogr., Sect. A: Found. Crystallogr. **A61**, 3 (2005).
[29] R. Oppermann and H. Thomas, Z. Phys. B **22**, 387 (1975).
[30] F. Birch, J. Geophys. Res. **83**, 1257 (1978).
[31] L. Stixrude, J. Geophys. Res., [Solid Earth] **107**, (2002).
[32] E. K. H. Salje, M. C. Gallardo, J. Jimenez, F. J. Romero, and J. del Cerro, J. Phys.: Condens. Matter **10**, 5535 (1998).
[33] J. P. Watt, G. F. Davies, and R. J. O. Connell, Rev. Geophys. Space Phys. **14**, 541 (1976).
[34] R. M. Wentzcovitch, B. B. Karki, M. Cococcioni, and S. de Gironcoli, Phys. Rev. Lett. **92**, 018501 (2004).
[35] L. Stixrude and C. Lithgow-Bertelloni, Geophys. J. Int. **162**, 610 (2005).
[36] R. J. Angel, J. Zhao, and N. L. Ross, Phys. Rev. Lett. **95**, 025503 (2005).
[37] B. Okai and J. Yoshimoto, J. Phys. Soc. Jpn. **39**, 162 (1975).

[38] R. J. Harrison, S. A. T. Redfern, and J. Street, Am. Mineral. **88**, 574 (2003).
[39] K. Fossheim and B. Berre, Phys. Rev. B **5**, 3292 (1972).
[40] W. A. Dollase, J. Appl. Crystallogr. **19**, 267 (1986).
[41] A. March, Z. Kristallogr. **81**, 285 (1932).
[42] T. Kurashina, K. Hirose, S. Ono, N. Sata, and Y. Ohishi, Phys. Earth Planet. Inter. **145**, 67 (2004).
[43] L. Li, D. J. Weidner, J. P. Brodholt, D. Alfe, G. D. Price, R. Caracas, and R. Wentzcovitch, Phys. Earth Planet. Inter. (to be published).
[44] D. J. Adams and A. R. Oganov, Phys. Rev. B **73**, 184106 (2006).
[45] C. J. Howard, K. S. Knight, B. J. Kennedy, and E. H. Kisi, J. Phys.: Condens. Matter **12**, L677 (2000).
[46] B. J. Kennedy, B. A. Hunter, and J. R. Hester, Phys. Rev. B **65**, 224103 (2002).
[47] J. R. Hester, C. J. Howard, B. J. Kennedy, and R. Macquart, Aust. J. Chem. **55**, 543 (2002).
[48] B. J. Kennedy, K. Yamaura, and E. Takayama-Muromachi, J. Phys. Chem. Solids **65**, 1065 (2004).
[49] H. Fujimori, M. Kakihana, K. Ioku, S. Goto, and M. Yoshimura, J. Ceram. Soc. Jpn. **112**, 189 (2004).
[50] E. H. Mountstevens, S. A. T. Redfern, and J. P. Attfield, Phys. Rev. B **71**, 220102 (2005).
[51] L. Li, D. J. Weidner, J. P. Brodholt, D. Alfe, G. D. Price, R. Caracas, and R. Wentzcovitch, Phys. Earth Planet. Inter. (to be published).
[52] H. Kawakatsu and F. L. Niu, Nature (London) **371**, 301 (1994).
[53] L. Vinnik, M. Kato, and H. Kawakatsu, Geophys. J. Int. **147**, 41 (2001).
[54] G. Masters, G. Laske, H. Bolton, and A. Dziewonski, in *Earth's Deep Interior: Mineral Physics and Tomography from the Atomic to the Global Scale*, edited by S. Karato, A. M. Forte, R. C. Liebermann, G. Masters, and L. Stixrude (American Geophysical Union, Washington, DC, 2000), pp. 63–88.
[55] A. V. G. Chizmeshya, G. H. Wolf, and P. F. McMillan, Geophys. Res. Lett. **23**, 2725 (1996).
[56] A. M. Glazer, Acta Crystallogr., Sect. B: Struct. Crystallogr. Cryst. Chem. **B28**, 3384 (1972).
[57] C. J. Howard and H. T. Stokes, Acta Crystallogr., Sect. B: Struct. Sci. **B58**, 565 (2002).
[58] A. M. Dziewonski and D. L. Anderson, Phys. Earth Planet. Inter. **25**, 297 (1981).
[59] M. Akaogi, M. Yano, Y. Tejima, M. Iijima, and H. Kojitani, Phys. Earth Planet. Inter. **143-44**, 145 (2004).
[60] A. Zerr, G. Serghiou, and R. Boehler, Geophys. Res. Lett. **24**, 909 (1997).
[61] J. M. Brown and T. J. Shankland, Geophys. J. R. Astron. Soc. **66**, 579 (1981).
[62] W. Kraus and G. Nolze, J. Appl. Crystallogr. **29**, 301 (1996).